

# Input Harmonic Controlled Broadband Continuous Class-F Power Amplifiers for Sub-6 GHz 5G Applications

Sagar K. Dhar, Tushar Sharma, *Student Member, IEEE*, Ning Zhu, Ramzi Darraji, Roy McLaren, Damon G. Holmes, *Member, IEEE*, Vince Mallette, and Fadhel M. Ghannouchi, *Fellow, IEEE*

**Abstract**—A comprehensive analysis is presented for investigating the effects of input nonlinearity on performance and broadband design of continuous mode class-F power amplifiers (PAs). New time-domain waveforms are derived considering input and output harmonic terminations for continuous mode class-F operation. The derived design equations show that the typical fundamental load design space of a continuous class-F PA must be re-engineered in presence of second harmonic input nonlinearity to a new design space in order to achieve optimum class-F PA performance versus varying second harmonic load impedance. For the practical validation, the impacts of input nonlinearity on the performance of continuous-mode class-F PAs are first confirmed with pulsed vector load pull (VLP) measurements on a low power GaN 2 mm device. Second, a broadband high power GaN 24 mm part is designed following the proposed theory with in-package input second harmonic terminations targeting 1.75-2.3 GHz frequency band for sub-6 GHz 5G high-power applications. Efficiency higher than 65% with peak power more than 53.2 dBm was maintained over the target frequency band, with excellent flatness. Third, a Doherty PA is implemented based on the designed GaN 24 mm part to evaluate the broadband performance with modulated stimuli. Using a multi-carrier signal having an instantaneous bandwidth of 395 MHz, the average drain efficiency of the Doherty PA at 8 dB output back-off is higher than 44% and the linearized adjacent channel power ratio (ACPR) is better than -52 dBc.

**Index Terms**— Broadband, class-F, continuous class-F, Doherty, high power, input nonlinearity, multi-harmonic load pull, power amplifier, waveform engineering.

## I. INTRODUCTION

POWER AMPLIFIERS (PAs) play a crucial role in overall radio frequency (RF) front-end system efficiency performance. Being the most power-hungry device in the system, high efficiency PA not only reduces the power consumption, also lowers the cooling system requirements. Consequently, the pursuit of high efficiency PAs and their design techniques has been ongoing. The fundamental understanding of high

efficiency PA design techniques can be trailed down to the 1920s [1] and in this century long journey, not only the power devices have been evolved from vacuum tube to high power density solid state ones, output load networks are also explored extensively from tuned load (TL) to bi-harmonic, poly-harmonic or in general to harmonic tuned (HT) ones [2].

In the HT PAs [3]–[10], harmonic load terminations are configured such that voltage and current waveforms are shaped with minimum overlapping in order to generate minimum harmonic power. This leads to the rectangular and half sinusoidal voltage/current waveforms for class-F/F<sup>-1</sup> PA realized by terminating the even and odd harmonic loads at either short or open. Although fixed harmonic terminations make the PA load network design complex, they enhance the PA efficiency performance [11]. Considering the performance, size, and complexity of a practical implementation, it is common to design HT PAs up to third harmonic load terminations. However, due to the fixed terminations at fundamental and harmonics, these PA design techniques are for single frequency applications. To cope up with this limitation, continuous mode HT PAs have been proposed and well exercised [12]–[24] for a broadband operation where PA performance is maintained over the operating band.

The abovementioned design techniques assume a fixed short circuit harmonic termination at the intrinsic gate node under the fact that the input harmonic termination (especially second harmonic) other than a short can cause PA performance degradation due to input nonlinearity [25]–[28]. The basis of this conclusion is that the input second harmonic impedance ( $Z_{2s}$ ) termination other than a short circuit widens the drain current waveform and increases conduction angle which consequently reduces the PA efficiency performance. Although a fixed short circuit  $Z_{2s}$  termination nullifies the input nonlinearity, an absolute short is not possible to maintain in practice for a broadband operation. Moreover, there are possible  $Z_{2s}$  terminations that can also reduce the drain current

This work was supported in part by the National Research Council of Canada and in part by Alberta Innovates Technology Futures.

S. K. Dhar, and F. M. Ghannouchi are with the University of Calgary, Calgary, AB T2N 1N4, Canada (e-mail: sagar.dhar@ucalgary.ca; fadhel.ghannouchi@ucalgary.ca).

T. Sharma is with the Department of Electrical and Computer Engineering, Princeton University, Princeton, NJ 08544, USA (email: tsharm@princeton.edu).

N. Zhu, R. McLaren, and D. G. Holmes are with the NXP Semiconductors, Chandler, AZ 85224, USA (e-mail: ning.zhu@nxp.com; roy.mclaren@nxp.com; damon.holmes@nxp.com)

R. Darraji is with the Ericsson Canada Inc. Ottawa, ON K2K 2V6, Canada (email: ramzi.darraji@ericsson.com)

V. Mallette is with the Focus Microwaves, Montreal, QC H9B 3H7, Canada (email: vince@focus-microwaves.com)

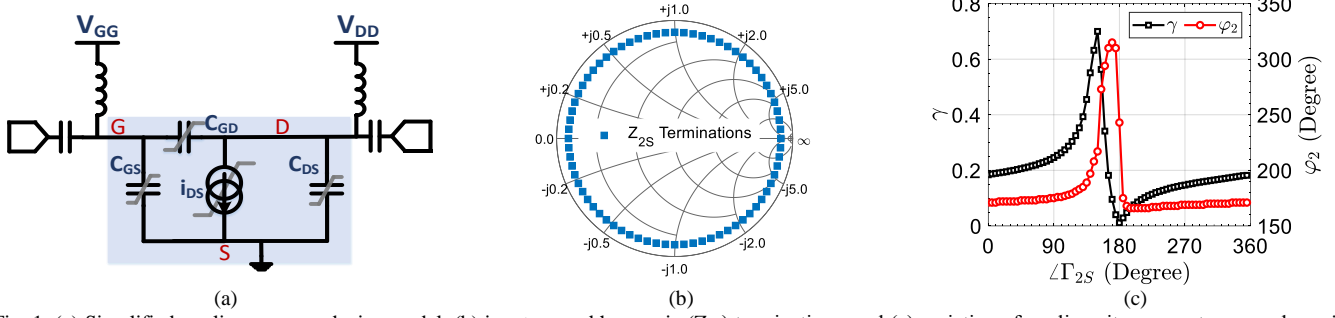


Fig. 1. (a) Simplified nonlinear power device model, (b) input second harmonic ( $Z_{2S}$ ) terminations, and (c) variation of nonlinearity parameters,  $\gamma$  and  $\varphi_2$  with  $Z_{2S}$  terminations.

conduction angle and improve PA performance [29]. As such, it is crucial to understand the impact of input nonlinearity on the input-output waveform shaping and on the PA performance. Although, the impact of input nonlinearity is investigated in [30]–[33], a complete analysis is still missing for continuous-mode class-F HT PAs.

In this work, a comprehensive analysis on the effects of input nonlinearity in continuous mode class-F PA operation is presented. Unlike continuous mode class-F<sup>-1</sup> PA [33], it is identified herein that a continuous class-F PA is greatly sensitive to the input nonlinearity and theoretical analysis shows that a distinct design strategy is required for continuous class-F operation in presence of input nonlinearity. We demonstrate that, due to the drain current waveform shaping by the input nonlinearity, the fundamental load design space must be re-engineered in order to recover and maintain the class-F PA continuum versus varying second harmonic load impedance. New comprehensive time-domain waveforms are also derived under input-output harmonic terminations for continuous class-F PA operation. Based on these waveforms, the generation of input nonlinearity is linked to the  $Z_{2S}$  termination to identify the favorable and adverse regions of the input second harmonic design space.

The rest of the paper is organized as follows. In Section II, the input nonlinearity generation and the theoretical analyses on its impacts on the continuous mode class-F operation are presented. The load pull validation of the theory is discussed in Section III. In Section IV, PA implementation and measurement results are reported. Finally, conclusions are drawn in Section V.

## II. CONTINUOUS CLASS-F WAVEFORM ENGINEERING THEORY

Input and output nonlinearity shape the input and output waveforms of a PA and influence its performance. In this section, input-output nonlinearities and their impacts on continuous class-F PAs are discussed analytically.

### A. Input Nonlinearity Generation

Input nonlinearity is typically introduced by the nonlinear  $C_{GS}$ - $v_{GS}$  profile of a power device. It generates harmonic voltage components at the gate node. Considering up to second harmonics, the gate voltage can be expressed as

$$v_{GS}(\theta) = V_{GS0} + V_1 \cos \theta + V_2 \cos(2\theta + \varphi_2)$$

$$v_{GS, \text{norm}}(\theta, \gamma, \varphi_2) = \frac{v_{GS}(\theta) - V_{GS0}}{V_1} = \cos \theta + \gamma \cos(2\theta + \varphi_2) \quad (1)$$

where input nonlinearity parameter  $\gamma = V_2/V_1$  is the ratio between the fundamental and second harmonic gate voltage components,  $\varphi_2$  indicates the phase difference, and  $V_{GS0}$ ,  $v_{GS, \text{norm}}$  are the gate bias voltage, and the normalized gate voltage, respectively.

To assess the input nonlinearity generation in terms of  $\gamma$  and  $\varphi_2$ , a simplified nonlinear large-signal model of a GaN 2 mm device is considered as in Fig. 1(a) based on a drain current equation with parameters that adequately describes measured DC I-V as a function of  $V_{GS}$  and  $V_{DS}$ . The nonlinear  $C_{GS}$ ,  $C_{GD}$  and  $C_{DS}$  profiles are extracted as functions of  $V_{GS}$ ,  $V_{GD}$ , and  $V_{DS}$ , respectively, and implemented as 1-D splines within the circuit simulator. The model is driven into saturation while sweeping  $Z_{2S}$  around the edge of the Smith chart ( $|\Gamma_{2S}|=0.9$ ) with a step of  $5^\circ$  as shown in Fig. 1(b). The simulations are performed at 1 GHz with fundamental source ( $Z_{1S}$ ) conjugate matched, fundamental load ( $Z_{1L}$ ) terminated at maximum efficiency point (MXE), and load harmonics ( $Z_{2L}$ ,  $Z_{3L}$ ) short circuited. The recorded  $\gamma$  and  $\varphi_2$  are shown in Fig. 1(c). With different  $Z_{2S}$  terminations,  $\gamma$  changes up to 0.7 which indicates significant second harmonic voltage generation (up to 70% compared to the fundamental) by intrinsic device nonlinearity. On the other hand,  $\varphi_2$  is found to vary between  $\sim 170^\circ$  to  $\sim 320^\circ$ , contrasting with previous works [25]–[28] where  $\varphi_2$  is considered only to be  $180^\circ$ . For  $|\Gamma_{2S}|$  value lower than 0.9, the peak to peak variation of  $\gamma$  and  $\varphi_2$  is gradually decreased and converges to  $\gamma \approx 0.2$  and  $\varphi_2 \approx 170^\circ$ .

The input nonlinearity shapes the gate voltage waveforms based on the  $\gamma$  and  $\varphi_2$  which consequently shapes the drain current by the device transconductance. For different  $\gamma$  and  $\varphi_2$  values, the normalized gate voltage waveforms are shown in Fig. 2(a). It should be noted that the zero-level in Fig. 2(a) indicates the gate bias  $V_{GS0}$ . Thus, the zero level crossing indicates the conduction angle of the device in a class-B bias condition ( $V_{GS0} = V_P$ , pinch of voltage). It can be seen that the shape of the gate voltage waveform as well as the conduction angle are modified significantly by  $\gamma$  and  $\varphi_2$  values. The modified conduction angle,  $\beta$ , for a class-B bias condition can be found by solving

$$\cos \frac{\beta}{2} + \gamma \cos(\beta + \varphi_2) = 0 \quad (2)$$

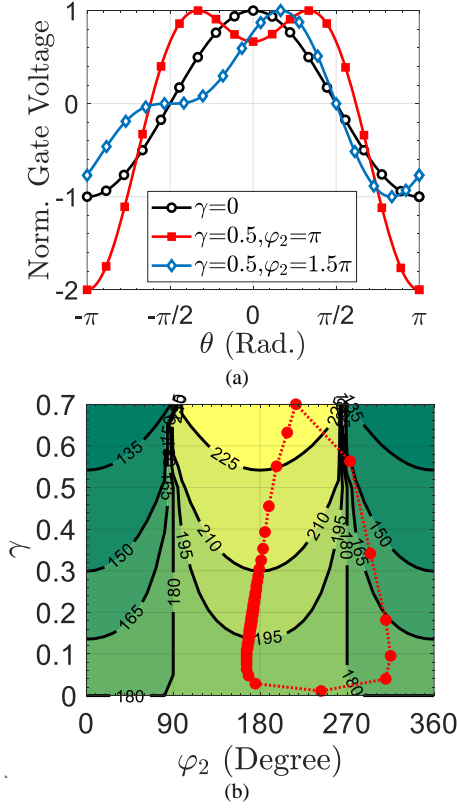


Fig. 2. (a) Gate voltage waveforms (normalized to  $V_{GSmax}$ ), and (b) calculated  $\beta$  along with the simulated  $\gamma$  and  $\varphi_2$  combinations (red dotted line) by input nonlinearity.

The variation of  $\beta$  with  $\gamma$  and  $\varphi_2$  values is shown in Fig. 2(b). The red dotted curve in Fig. 2(b) indicates model simulated  $\gamma$  and  $\varphi_2$  values for the GaN 2 mm device that are depicted in Fig. 1(c). It can be seen that the conduction angle can increase to  $\sim 225^\circ$  or reduce to  $\sim 160^\circ$  compared to the nominal bias conduction angle of  $180^\circ$ . The input nonlinearity parameters for a few key points are summarized in Table I. The modified conduction angle  $\beta$  converges to  $180^\circ$  as expected when  $Z_{2S}$  is short circuited (Case I). The maximum device conduction angle occurs at  $\angle\Gamma_{2S} = 150^\circ$  (Case II) and the minimum at  $\angle\Gamma_{2S} = 160^\circ$  (Case III). Such deviation in conduction angle is translated into efficiency performance variation due to input nonlinearity.

### B. Continuous Class-F Drain Current Waveforms

For a typical continuous class-F PA, the third harmonic load ( $Z_{3L}$ ) is terminated at open circuit and the second harmonic load ( $Z_{2L}$ ) is swept near short. Due to the open circuit termination, the third harmonic current cannot sustain and the drain current waveform remains half sinusoidal for a typical continuous class-F PA ( $Z_{2S} = 0$ ). Considering both input nonlinearity and open circuit  $Z_{3L}$  termination, the continuous class-F drain current waveform is defined as

$$i_{DS,ICF}(\theta, \gamma, \varphi_2) = \begin{cases} \varepsilon[\cos \theta + \gamma \cos(2\theta + \varphi_2)] - (\chi \cos 3\theta - \xi \sin 3\theta), & -\frac{\beta}{2} \leq \theta \leq \frac{\beta}{2} \\ 0, & -\pi \leq \theta \leq -\frac{\beta}{2}, \frac{\beta}{2} \leq \theta \leq \pi \end{cases} \quad (3)$$

TABLE I  
SIMULATED INPUT NONLINEARITY PARAMETERS OF A GAN 2 MM  
DEVICE AT 1 GHz, AND  $|\Gamma_{2S}| = 0.9$

$\angle\Gamma_{2S}$ (Degree)	$\gamma$	$\varphi_2$ (Degree)	$\beta$ (Degree)
180 (Case I)	0	-	180
150 (Case II)	0.7	217	228
160 (Case III)	0.34	294	161

where  $\chi, \xi$  denote the coefficients for real and reactive terms of third harmonic drain current,  $i_3 = \chi \cos 3\theta - \xi \sin 3\theta$ , respectively. The subtraction of  $i_3$  in (3) reflects the impact of open circuit  $Z_{3L}$  termination by current trapping technique [7], [20]. This paper introduces a current limiting factor  $\varepsilon$  to prevent drain current exceeding maximum drain current  $I_{max}$ . Thus, the current limiting factor is calculated by setting  $i_{DS,ICF}(\max) = I_{max}$  and solved as

$$\varepsilon(\gamma, \varphi_2) = \frac{I_{max} + \chi \cos 3\theta_m - \xi \sin 3\theta_m}{\cos \theta_m + \gamma \cos(2\theta_m + \varphi_2)} \quad (4)$$

where  $\theta_m$  is the phase at which  $i_{DS,ICF} = I_{max}$ . The third harmonic current components  $\chi, \xi$  are computed by setting the real and reactive current component to be zero as

$$I_{3r}(\beta, \gamma, \varphi_2) = \frac{1}{\pi} \int_{-\beta/2}^{+\beta/2} i_{DS,ICF}(\theta, \gamma, \varphi_2) \cdot \cos 3\theta \, d\theta = 0 \quad (5a)$$

$$I_{3q}(\beta, \gamma, \varphi_2) = \frac{1}{\pi} \int_{-\beta/2}^{+\beta/2} i_{DS,ICF}(\theta, \gamma, \varphi_2) \cdot \sin 3\theta \, d\theta = 0 \quad (5b)$$

Thus, the Fourier drain current components are computed from (3) as

$$I_{DC}(\beta, \gamma, \varphi_2) = \frac{\varepsilon}{\pi} \left[ \sin \frac{\beta}{2} + \frac{\gamma \cos \varphi_2}{2} \sin \beta \right] - \frac{\chi}{3\pi} \sin \frac{3\beta}{2} \quad (6)$$

$$I_{1r}(\beta, \gamma, \varphi_2) = \frac{\varepsilon}{2\pi} (\beta + \sin \beta) - \frac{\chi [\sin 2\beta + 2 \sin \beta]}{4\pi} + \frac{\varepsilon \gamma \cos \varphi_2}{3\pi} \left[ 3 \sin \frac{\beta}{2} + \sin \frac{3\beta}{2} \right] \quad (7)$$

$$I_{1q}(\beta, \gamma, \varphi_2) = \frac{\xi}{4\pi} (2 \sin \beta - \sin 2\beta) - \frac{\varepsilon \gamma \sin \varphi_2}{3\pi} \left[ 3 \sin \frac{\beta}{2} - \sin \frac{3\beta}{2} \right] \quad (8)$$

$$I_{2r}(\beta, \gamma, \varphi_2) = \frac{\varepsilon}{\pi} \left[ 2 \sin \frac{\beta}{2} - \frac{4}{3} \sin^3 \frac{\beta}{2} + \gamma \cos \varphi_2 \frac{2\beta + \sin 2\beta}{4} \right] - \frac{\chi}{\pi} \left( \sin \frac{\beta}{2} + \frac{1}{5} \sin \frac{5\beta}{2} \right) \quad (9)$$

$$I_{2q}(\beta, \gamma, \varphi_2) = \frac{4\xi}{\pi} \left( \sin^3 \frac{\beta}{2} - \frac{4}{5} \sin^5 \frac{\beta}{2} \right) - \frac{\varepsilon \gamma \sin \varphi_2 (2\beta - \sin 2\beta)}{4\pi} \quad (10)$$

where  $I_{DC}$ ,  $I_{1r}$ , and  $I_{2r}$  are the DC, fundamental and second harmonic real drain current components, respectively, and  $I_{1q}$ ,  $I_{2q}$  are the fundamental, and second harmonic reactive drain current components, respectively.

With the Fourier coefficients calculated, the reconstructed drain current waveforms for the three cases mentioned in Table I are shown in Fig. 3. As expected, the drain current waveform for Case I is half sinusoidal resembling to the typical continuous class-F one with  $180^\circ$  device conduction angle since

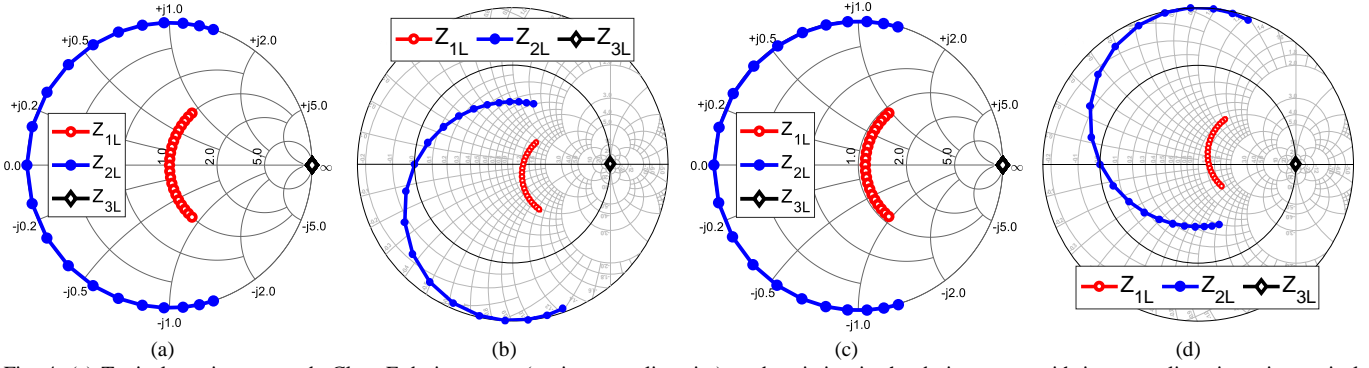


Fig. 4. (a) Typical continuous mode Class F design space (no input nonlinearity), and variation in the design space with input nonlinearity using typical continuous Class F drain voltage waveform at (b)  $\gamma = 0.7$ ,  $\phi_2 = 0.5\pi$ , (c)  $\gamma = 0.7$ ,  $\phi_2 = \pi$ , and (d)  $\gamma = 0.7$ ,  $\phi_2 = 1.5\pi$ .

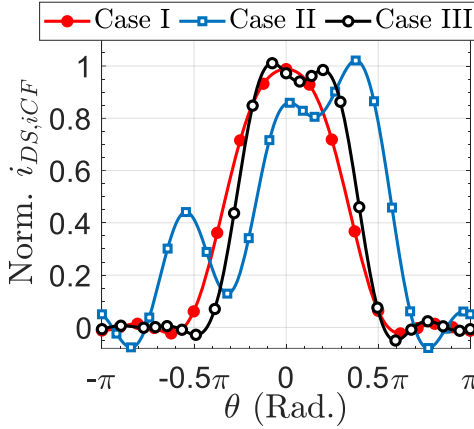


Fig. 3. Normalized continuous Class F drain current waveforms with input nonlinearity. [Normalized to  $I_{\max}$ ]

input nonlinearity factor  $\gamma = 0$ . This ensures the accuracy of the analyses. Besides, the device conduction angle increases for Case II and decreases for Case III, as anticipated.

### C. Continuous Class-F Drain Voltage Waveforms

For the class-F PA operation over a frequency band, continuous mode PA was introduced [12]–[15]. The drain voltage waveform is defined as

$$v_{DS,CF}(\theta) = V_{DD} - \frac{2}{\sqrt{3}}(V_{DD} - V_K) \left( \cos \theta - \frac{1}{6} \cos 3\theta \right) (1 - \delta \sin \theta) \quad (11)$$

where  $V_{DD}$ , and  $V_K$  are the drain supply voltage, and knee voltage, respectively. In a classical continuous class-F (CCCF) PA operation, the theoretical output power and efficiency performance is maintained over a  $Z_{1L}$  and  $Z_{2L}$  design space which can be computed from (3) and (11) as

$$Z_{nL} = -\frac{V_{nr} - V_{nq}}{I_{nr} - I_{nq}} \quad (12)$$

where  $Z_{nL}$  is the  $n^{\text{th}}$ -harmonic load impedance termination, and  $V_{nr}$ ,  $V_{nq}$  are the  $n^{\text{th}}$ -harmonic real and reactive drain voltage components, respectively. The design space for a CCCF PA is shown in Fig. 4(a). It is worth noting here that the input harmonics are assumed short circuited for a CCCF PA. In reality, however, it is not possible to maintain a short circuit termination over a frequency band. As such, input nonlinearity is inevitable and it is important to assess its impact on the CCCF

PA design space. For a few  $\gamma$  and  $\phi_2$  values, the variation of CCCF design space considering the classical drain voltage expression in (11) is illustrated in Fig. 4(b-d). Unfortunately, the drain voltage in (11) cannot result in purely reactive  $Z_{2L}$  terminations, in fact, it can lead to negative or resistive terminations in presence of input nonlinearity. This is due to the nonzero second harmonic reactive drain current components ( $I_{2q}$ ) generated by input nonlinearity as expressed in (10). Nevertheless, a designer can have the freedom of selecting purely reactive  $Z_{2L}$  terminations. Thus, the drain voltage waveform defined by (11) for CCCF PA operation is not suitable in presence of input nonlinearity. Accordingly, it is more appropriate to derive the drain voltage waveforms correspond to the  $Z_{2L}$  terminations selected by the designer. In this work, a time-domain drain voltage analysis of a continuous class-F PA is presented with arbitrary input and output second harmonic terminations. The impact of  $Z_{2S}$  termination on the drain voltage waveform is reflected through the current components which are functions of  $\gamma$  and  $\phi_2$ .

To derive new time-domain drain voltage waveform, fundamental and second harmonic voltage and current components can be related to the load terminations as

$$Z_{1L} = R_1 + jX_1 = -\frac{V_{1r} - V_{1q}}{I_{1r} - I_{1q}} \quad (13a)$$

$$Z_{2L} = jX_2 = -\frac{V_{2r} - V_{2q}}{I_{2r} - I_{2q}} \quad (13b)$$

$$Z_{3L} = -\frac{V_{3r} - V_{3q}}{I_{3r} - I_{3q}} = \infty \quad (13c)$$

and the modified generic drain voltage waveform can be defined as

$$v_{DS,CF(mod)}(\theta) = V_{DD} + V_{1r} \cos \theta + V_{1q} \sin \theta + V_{2r} \cos 2\theta + V_{2q} \sin 2\theta + V_{3r} \cos 3\theta \quad (14)$$

where  $V_{1r}$ ,  $V_{1q}$ ,  $V_{2r}$ ,  $V_{2q}$ , and  $V_{3r}$  are the fundamental real, reactive, second harmonic real, reactive, and third harmonic real voltage components, respectively. By equating the real and imaginary coefficients, the drain voltage components can be defined as

$$V_{1r} = -(I_{1q}X_1 + I_{1r}R_1) \quad (15a)$$

$$V_{1q} = I_{1r}X_1 - I_{1q}R_1 \quad (15b)$$

$$V_{2r} = -I_{2q}X_2 \quad (15c)$$



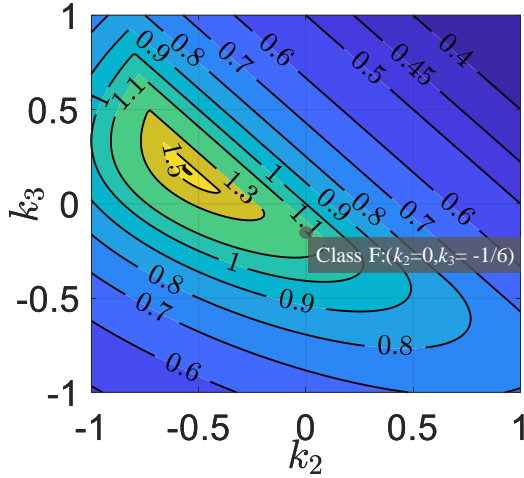


Fig. 5. Variation of fundamental voltage gain function  $\Delta(k_2, k_3)$ .

$$V_{2q} = I_{2r} X_2 \quad (15d)$$

To determine the drain voltage coefficients, there are a few conditions to be fulfilled, considering arbitrary selection of  $X_2$  around short circuit by the designer:

*Condition 1:* Since  $V_{2r} \neq 0$  as in (15c) unlike CCCF PA operation,  $V_{1r}$  value must be set such that the drain voltage,  $v_{DS,CF(mod)}$  remains non-negative.

*Condition 2:* Since  $V_{2q} \neq 0$  as in (15d),  $V_{1q}$  value should be determined such that  $v_{DS,CF(mod)}$  remains non-negative.

*Condition 3:* Sweeping  $X_2$  near short results in drain voltage peaking. Thus, a limit of absolute  $X_2$  value ( $X_{2,lim}$ ) has to be determined based on the allowable maximum drain voltage.

To find the relationship between  $V_{1r}$  and  $V_{2r}$ , a generic drain voltage of a HT PA can be considered as [2]

$$v_{DS,HT}(\theta) = V_{DD} - [V_{1r} \cos \theta + V_{2r} \cos 2\theta + V_{3r} \cos 3\theta] \quad (16a)$$

$$v_{DS,HT,norm}(\theta) = -\cos \theta - k_2 \cos 2\theta - k_3 \cos 3\theta \quad (16b)$$

where  $k_2, k_3$  are the normalized second and third harmonic real voltage components with respect to the fundamental. For different values of  $k_2$  and  $k_3$ , a fundamental HT PA voltage gain function is defined as [2]

$$\Delta(k_2, k_3) = \frac{V_{1r}}{V_{DD} - V_k} \quad (17)$$

and illustrated in Fig. 5, satisfying the condition  $[v_{DS,HT}(\theta)]_{\min} = 0$  or  $[v_{DS,HT,norm}(\theta)]_{\min} = -1$ . For a classical class-F (CCF) operation,  $k_2 = 0$  and  $k_3 = -1/6$  result in voltage gain function  $\Delta(k_2, k_3) = 2/\sqrt{3}$  and the well-known rectangular drain voltage waveform. To emphasize Condition 1, the generic drain voltage in (14) can be re-written by utilizing (16) and (17) as

$$v_{DS,CF(mod)}(\theta) = V_{DD} - \Delta(k_2, k_3)(V_{DD} - V_k)[\cos \theta + k_3 \cos 3\theta] + V_{1q} \sin \theta + V_{2r} \cos 2\theta + V_{2q} \sin 2\theta \quad (18)$$

The generic drain voltage in (18) presents an infinite number of solutions based on the combinations of  $k_2$  and  $k_3$ . However, an optimum constant  $k_3 = -1/6$  is considered in this analysis to start with the well-known rectangular CCF voltage waveform when

$Z_{2L} = jX_2 = 0$ . By equating (14) and (18), third harmonic voltage component can be defined as  $V_{3r} = -k_3 \Delta(k_2, k_3) (V_{DD} - V_k)$ .

To find the drain voltage waveforms for an arbitrary  $X_2$  value, first of all,  $V_{2r}$  and  $V_{2q}$  are calculated according to (15c) and (15d). Then, the voltage gain function  $\Delta(k_2, k_3)$  is mapped based on the  $k_2$  and  $k_3$  value. Once  $\Delta(k_2, k_3)$  is known for the given  $X_2$  value,  $V_{1r}$  can be calculated from (17). Afterwards, the only remaining coefficient  $V_{1q}$  is determined from (18) as a function of  $V_{2q}$  such that  $[v_{DS,CF(mod)}(\theta)]_{\min} = 0$ . This way, the drain voltage for an arbitrary second harmonic load termination can be determined with input nonlinearity. Although, there is no closed form solution for  $V_{1q}$ , an approximated linear relationship can be developed from the numerical solutions as

$$V_{1q} \approx -\sqrt{3}V_{2q}; k_3 = -\frac{1}{6} \quad (19)$$

Once the voltage coefficients are known, the equivalent fundamental real ( $R_1$ ) and reactive ( $X_1$ ) terminations can be determined as a function of  $X_2$  as

$$R_1 = \frac{\sqrt{3}I_{2r}X_2 + I_{1r}X_1}{I_{1q}} \quad (20)$$

$$X_1 = \frac{I_{1q}(V_{DD} - V_k)\Delta(k_2, k_3) - \sqrt{3}I_{1r}I_{2r}X_2}{I_{1r}^2 + I_{1q}^2} \quad (21)$$

The design spaces at different input nonlinearity conditions are shown in Fig. 6(a-d). Compared to the design space in Fig. 4, optimum fundamental load ( $Z_{1L}$ ) impedance is readjusted in Fig. 6 to adopt purely reactive  $Z_{2L}$  terminations. It can be seen that the optimum fundamental impedance at  $X_2 = 0$  illustrated in Fig. 6 as  $Z_{OPT,IF}$  is not always resistive due to the input nonlinearity. To obtain the optimum rectangular drain voltage waveform at  $X_2 = 0$ ,  $Z_{OPT,IF}$  is changed accordingly.

Finally, it is also important to evaluate the  $X_{2,lim}$  for a given limit of drain voltage maximum,  $v_{DS,max,lim}$ . As it is well-known, a change in  $X_2$  near short causes voltage peaking from its initial value of  $2 \times V_{DD}$ . It has been observed that the maximum drain voltage changes linearly with  $|X_2|$ . Thus,  $X_{2,lim}$  can be defined for different input nonlinearity parameters by finding the slope of such linear variations for the allowed drain voltage maximum ( $v_{DS,max,lim}$ ). For example, a linear relationship with  $\gamma = 0$  can be found as

$$X_{2,lim}(norm.) = \frac{7[v_{DS,max,lim} - 2V_{DD}]}{3V_{DD}}; \gamma = 0 \quad (22)$$

for  $v_{DS,max,lim} \geq 2V_{DD}$  where  $X_2$  is normalized by  $(V_{DD} - V_k)/I_{max}$ . With such limits, the new drain voltage waveforms for a few input nonlinearity conditions are shown in Fig. 6(e-h) for  $v_{DS,max,lim} = 3V_{DD}$ . It is worth noting that the drain voltage excursions are maintained above zero for second harmonic load sweep near short as conditioned before. Also, the rectangular drain voltage waveforms are maintained for different input nonlinearity conditions at  $X_2 = 0$  as expected.

To evaluate the PA performance, output power and efficiency are calculated as

$$P_{DC}(\beta, \gamma, \varphi_2) = V_{DD} \times I_{DC} \quad (23)$$

$$P_{OUT}(\beta, \gamma, \varphi_2) = -\frac{1}{2} \times \text{Re}[V_1 \cdot I_1^*] \quad (24)$$

$$= -\frac{1}{2} (V_{1r}I_{1r} + V_{1q}I_{1q})$$

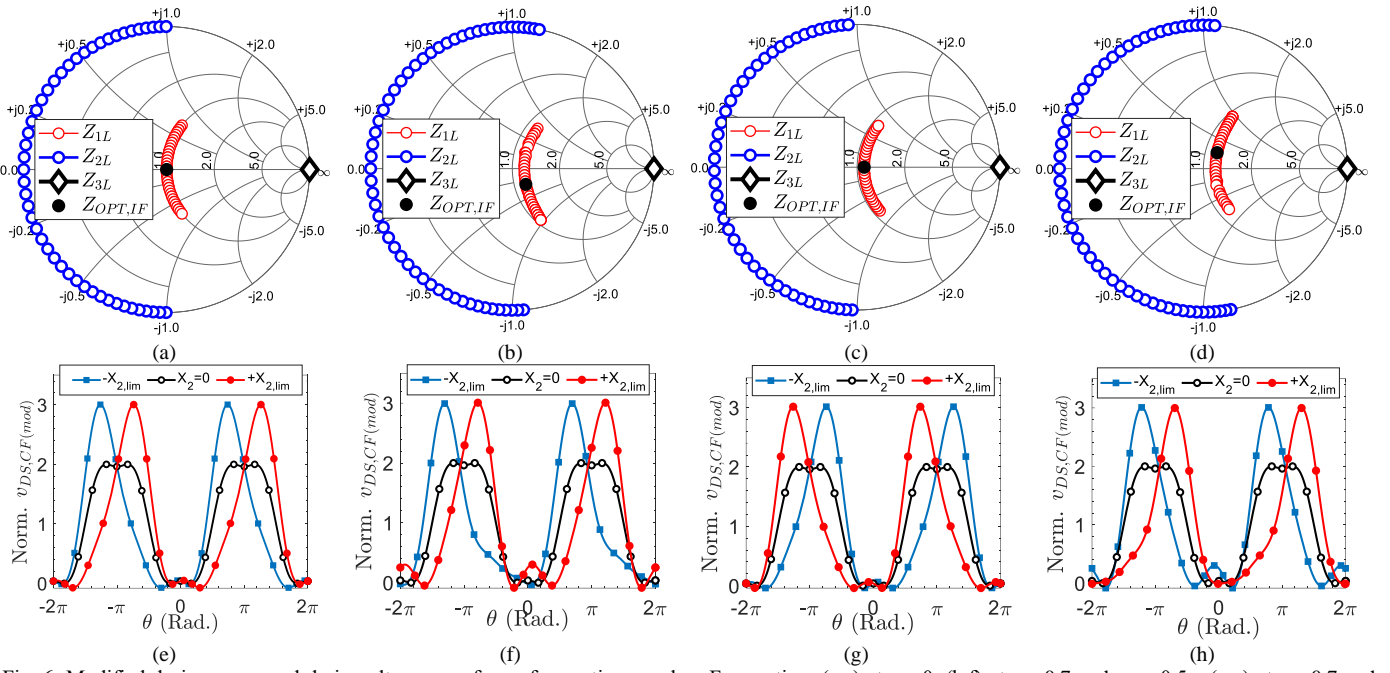


Fig. 6. Modified design space and drain voltage waveforms for continuous class F operation: (a,e) at  $\gamma = 0$ , (b,f) at  $\gamma = 0.7$  and  $\varphi_2 = 0.5\pi$ , (c,g) at  $\gamma = 0.7$  and  $\varphi_2 = 1\pi$ , and (d,h)  $\gamma = 0.7$  and  $\varphi_2 = 1.5\pi$ . [ $Z_0 = Z_{OPT,IF}(\gamma = 0)$  and  $v_{DS,CF(mod)}$  is normalized to  $V_{DD}$ ]

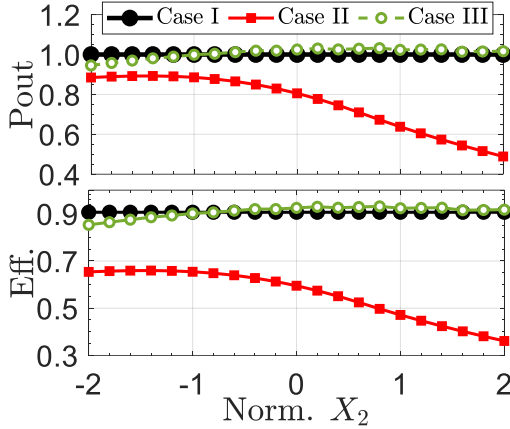


Fig. 7. Normalized output power and efficiency variation with second harmonic reactive load termination.

$$\eta(\beta, \gamma, \varphi_2) = \frac{P_{OUT}(\beta, \gamma, \varphi_2)}{P_{DC}(\beta, \gamma, \varphi_2)} \quad (25)$$

where  $I_1^*$  indicates the complex conjugate of the fundamental current. The variation of output power (normalized) and efficiency over  $X_2$  sweep near short for three cases of input nonlinearity is shown in Fig. 7. The output power is normalized to the typical class-F output power and the  $X_2$  value to  $(V_{DD} - V_k)/I_{max}$ . For Case I ( $\gamma = 0$ , no input nonlinearity), output power and efficiency are constant over  $X_2$  sweep, confirming the typical CCCF operation. For Case II (increased conduction angle), it is interesting to see that the efficiency is significantly decreased from the typical class-F one as anticipated due to higher conduction angle. More importantly, the efficiency and output power are not constant over  $X_2$  sweep unlike CCCF operation. The output power can drop by 3 dB from  $-X_2$  to  $+X_2$

point. Significant efficiency variation (65% to 35%) is also observed over  $X_2$  sweep for Case II. On the other hand, the variation of efficiency and output power for Case III is almost constant except few points higher or lower than the typical class-F ones. Conversely, one can see in Fig. 7 that Case III ( $\angle \Gamma_{2S} = 160^\circ$ ) with appropriate load terminations can provide the optimum continuous mode performance similar to CCCF operation.

### III. LOAD PULL MEASUREMENTS AND VALIDATION

#### A. Vector Load Pull (VLP) Measurement Setup

In this work, vector load pull (VLP) measurements are performed to validate the theoretical analyses presented. A VLP setup and measurement provide useful information about device input characteristics which enhances measurement accuracy compared to the conventional scalar load pull measurements. The setup mainly consists of a load tuner MPT 1808, a source tuner MPT Lite 1808 and a phase reference unit Mesuro PR-50 from Focus Microwaves Group, VNA ZVA67 and its extension unit ZVAX-TRM40 from Rohde & Schwarz, a spectrum analyzer MS2840A from Anritsu, and DC power supplies E3634A from Keysight. The load tuner can tune the fundamental ( $Z_{1L}$ ), second ( $Z_{2L}$ ) and third ( $Z_{3L}$ ) harmonic loads from 0.8 GHz to 18 GHz. The source tuner does the same for fundamental ( $Z_{1S}$ ) and second ( $Z_{2S}$ ) harmonic source impedances. To communicate, control and for synchronized measurements, Focus Device Characterization Suite (FDCS) [34] software is used. The setup mainly consists of two calibration steps. First, tuner calibration and then wave calibration. The tuners are calibrated with the FDCS software using VNA ZVA67. For wave calibration, Mesuro calibration software is used along with the Mesuro phase reference unit PR-50 and a power meter NRP2 with power sensor NRP Z57

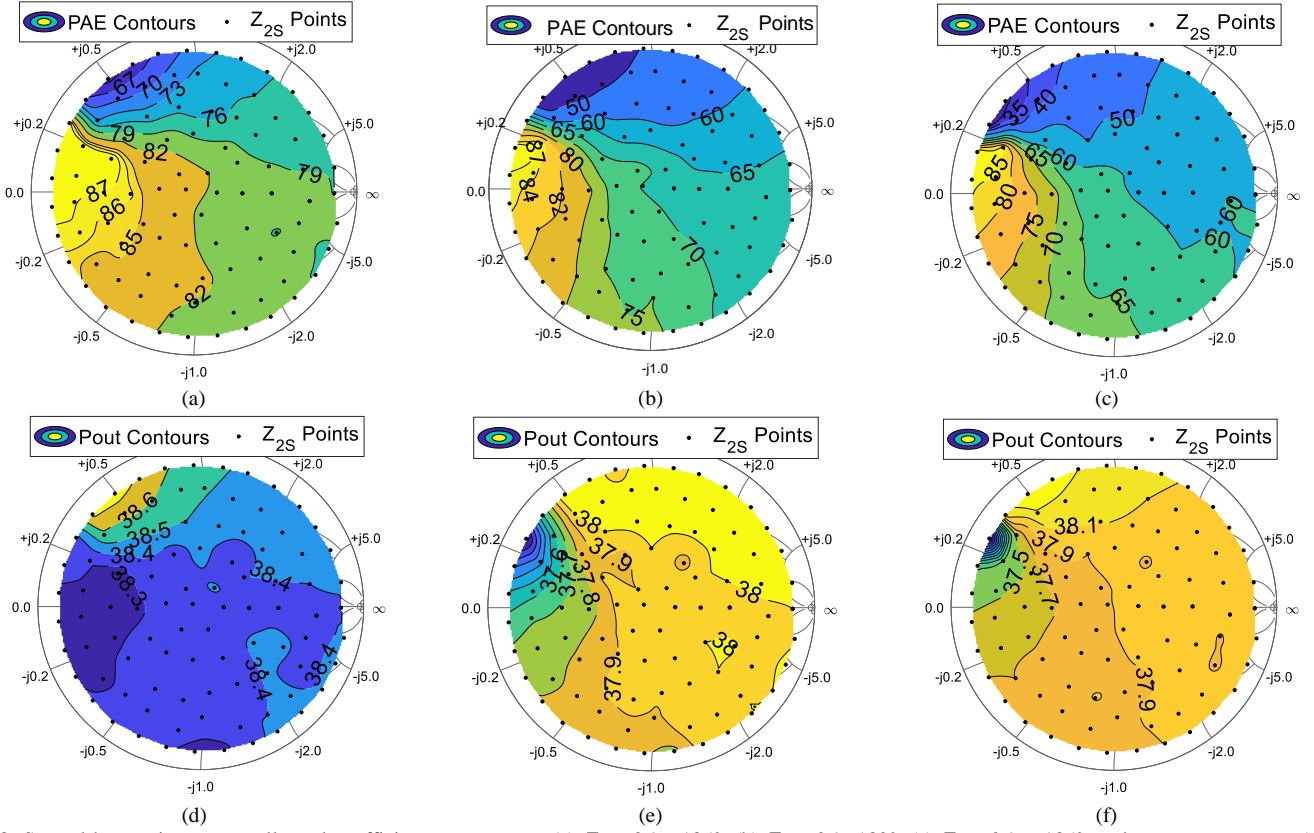


Fig. 8. Second harmonic source pull results: efficiency contours at (a)  $\Gamma_{2L} = 0.9\angle -135^\circ$ , (b)  $\Gamma_{2L} = 0.9\angle 180^\circ$ , (c)  $\Gamma_{2L} = 0.9\angle +135^\circ$ , and power contours at (d)  $\Gamma_{2L} = 0.9\angle -135^\circ$ , (e)  $\Gamma_{2L} = 0.9\angle 180^\circ$ , (f)  $\Gamma_{2L} = 0.9\angle +135^\circ$ . [ $Z_0 = 50 \Omega$ ]

from Rohde & Schwarz. For wave measurements, both wave power and phase calibration are performed by Mesuro calibration software and utilized in the FDSC wave load-pull measurement software.

For GaN device measurements, thermal effects play a vital role in performance metrics number. To validate the HT PA theory, the device is driven into saturation for repetitive measurements. If continuous wave (CW) large signal measurements are performed, GaN device performance are influenced significantly by thermal effects. To alleviate device heating and to avoid temperature effect, a pulsed wave load-pull measurement system is facilitated with a pulse modulator that comes with the ZVAX-TRM40 extension unit. Such pulsed VLP measurement ensures accurate and repeatable measurements in a quasi-isothermal environment.

### B. VLP Measurement Results

To validate the theoretical framework presented in the previous section, pulsed VLP measurements are performed with a GaN 2 mm device at 1 GHz. To perform accurate load pull measurements and to probe intrinsic parameters, however, device parasitics especially the drain to source capacitance ( $C_{DS}$ ) must be deembedded. To do so, efficiency minima phenomenon presented in [9] is utilized. Once the parasitic information is extracted, the impact of second harmonic source-pull is investigated at different fundamental and harmonic loading conditions of a continuous class-F mode of operation.

The second harmonic source pull results for three cases  $\Gamma_{2L} = 0.9\angle -135^\circ$  ( $X_2 = -20 \Omega$ ),  $\Gamma_{2L} = 0.9\angle 180^\circ$  ( $X_2 = 0$ ), and

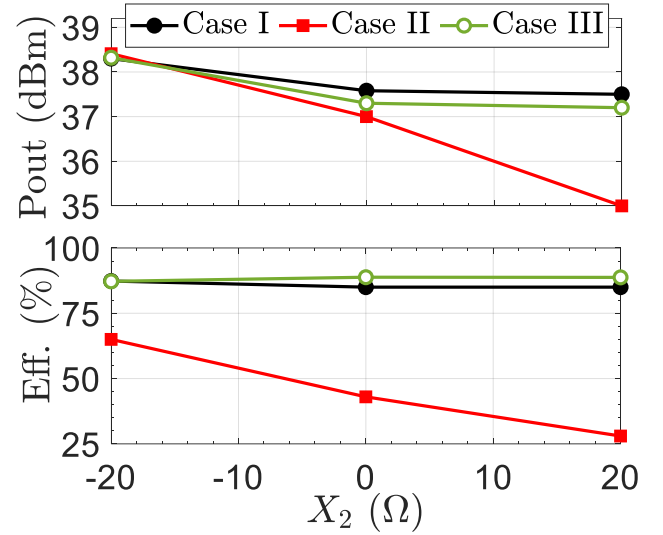


Fig. 9. Efficiency and output power performance with different nonlinearity conditions (Case I-III) of a continuous mode Class F PA operation,  $X_2 = -20$ , 0, and  $+20 \Omega$ .

$\Gamma_{2L} = 0.9\angle +135^\circ$  ( $X_2 = 20 \Omega$ ) are shown in Fig. 8. The fundamental load is terminated at MXE. The maximum  $|\Gamma_{2S}|$  realized at the intrinsic gate node is about 0.9 due to the loss of the couplers, coaxial cables, probes and device parasitics. Although a higher reflection coefficient is always desirable,  $|\Gamma_{2S}| \approx 0.9$  is enough to probe important source pull information. It is also a fair representative to a reflection coefficient that is most possibly implemented in a matching network in practice. As seen from Fig. 8(a-c), the efficiency performance of a

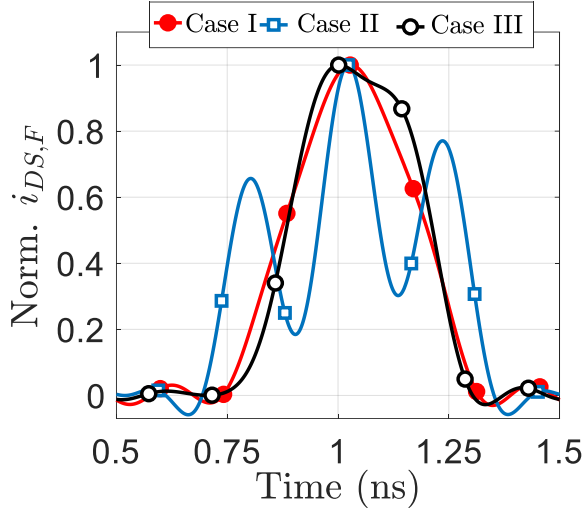


Fig. 10. Measured drain current waveforms with different input nonlinearity conditions.

continuous class-F PA is significantly impacted by the second harmonic source termination over the whole Smith chart. In all three measurements, it is clear that there is a certain area of intrinsic source second harmonic termination (around  $\angle\Gamma_{2S} = 140^\circ$ ) where efficiency degrades the most (identified as Case II in Table I). On the other hand, there are terminations around  $\angle\Gamma_{2S} = 160^\circ$  where efficiency is about 3% higher than a perfect short termination (identified as Case III in Table I). Overall, there is a range of  $Z_{2S}$  terminations from  $-j25\ \Omega$  to  $+j5\ \Omega$  (or in general the lower half of the Smith Chart) that can be identified for optimum continuous class-F operation with input nonlinearity where efficiency is degraded the least. Besides, it can be identified from the output power contours shown in Fig. 8(d-f) that the worst efficiency region ( $\angle\Gamma_{2S} = 140^\circ$ ) also provides the lowest output power performance. On the other hand, the output power in the better efficiency region is comparable to that of the conventional input second harmonic short termination one.

Moreover, it is interesting to observe from Fig. 8 that the efficiency and output power performance is not consistent for different  $X_2$  terminations as predicted analytically in Section IIC. To evaluate the performance variation, the output power and efficiency is plotted versus  $X_2$  terminations in Fig. 9. It can be seen that both the efficiency and output power are significantly varied for Case II and the continuity of a continuous class-F PA is greatly perturbed. On the other hand, Case I and Case III show relatively consistent performance over  $X_2$  variation. These measured results are in excellent agreement to the analytically predicted ones showed in Fig. 7.

The drain current waveforms for three different input nonlinearity cases are shown in Fig. 10 for  $X_2 = 0$ . At  $Z_{2S}$  short circuit condition (Case I), the drain current is a half sinusoidal waveform as expected for a class-F mode of operation. However, at the presence of input nonlinearity, current waveform is shaped. For Case II, the drain current conduction angle is increased and forms two additional side-peaks resembles quite well with the analytical prediction illustrated in Fig. 3. On the other hand, the drain current conduction angle is

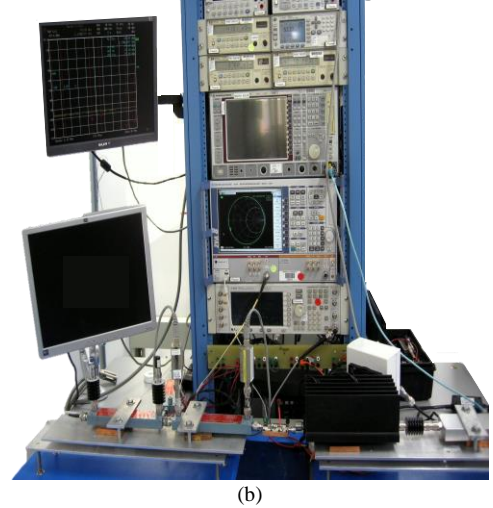
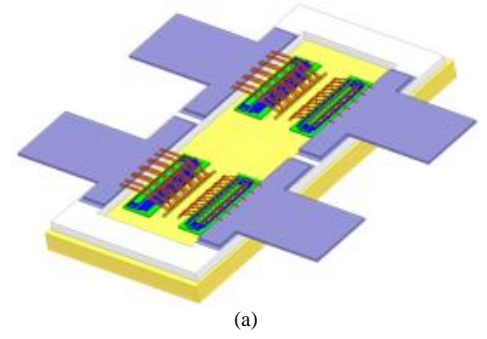


Fig. 11. (a) In-package input harmonic terminated prematched GaN 24 mm power device, and (b) high power measurement setup.

decreased for Case III compared to the Case I and Case II. This is in well agreement to the analytical prediction presented in Section IIB.

These source/load pull measurement results validate the theoretical framework presented in Section II. The analyses and measurement results show that the input harmonic energy can impact the efficiency and output power performance of a continuous class-F PA. The favorable and adverse design regions for  $Z_{2S}$  terminations are identified for continuous mode class-F operation. The variation of the continuous class-F PA performance with input nonlinearity is validated.

#### IV. PA IMPLEMENTATION, MEASUREMENT RESULTS, AND DISCUSSIONS

The load-pull validation presented in section III provides a comprehensive insight into the validity of the theoretical framework presented in the paper. Along with the low power GaN load-pull measurement this section presents an implementation of the input-output harmonic control for the design of a 24 mm high-power GaN device [35]. The theory is further validated by mounting this active die in a high power air cavity package with pre-matching network operating from 1.75-2.3 GHz for high-power macro base-station applications, as shown in Fig. 11(a). The in-package terminations are implemented using wirebond inductance and with the input and output integrated passive devices (IPDs) inside the package.



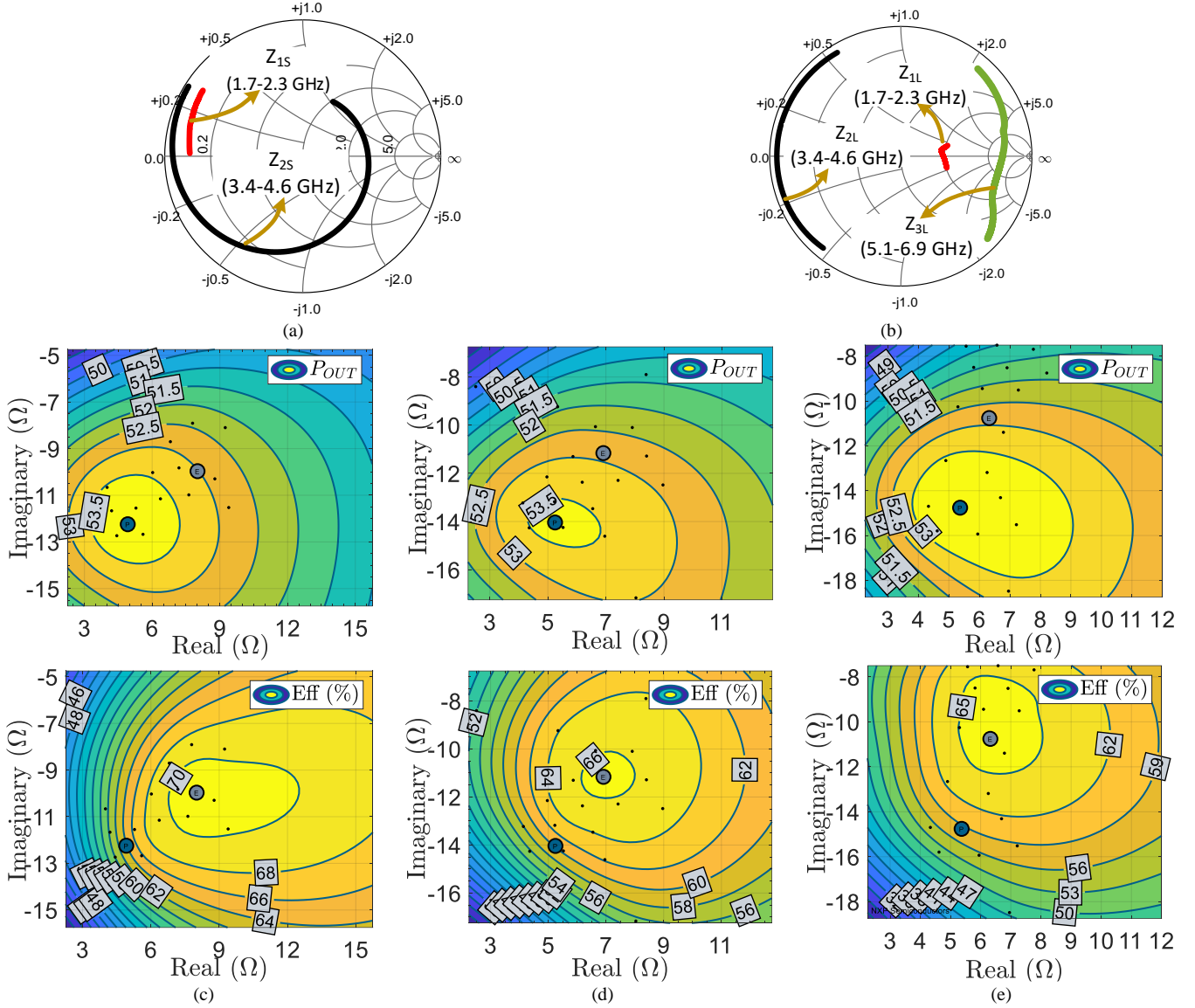


Fig.12. (a,b) Intrinsic design space ( $Z_0 = 3.5\Omega$ ) for 24 mm GaN part at source and load. Measured output power and drain efficiency contours for constant 3dB gain compression at (c) 1.88 GHz (d) 2.11 GHz and (e) 2.2 GHz.

The measurements are carried out using both continuous wave (CW) and modulated signals. The measurement setup is shown in Fig. 11(b) essentially consists of Rhode and Schwarz SMU200A modulated signal source which drives the device under test (DUT) through 50-W Amplifier Research (AR) driver with linear gain  $>45$  dB. The isolator is placed at the driver output to provide fixed  $50\Omega$  source impedance to the DUT and hence prevent any standing waves caused due to the mismatch between the driver and the DUT input. Effective input and output power of the DUT, coupled through the directional couplers, are measured using Keysight N1912B power meters with over 60-dB dynamic range capability. Rhode and Schwartz Spectrum Analyzer FSQ8 is also incorporated in the setup to compute ACPR from the captured PA output spectrum.

#### A. High Power GaN Pre-Match Implementation and Measurement Results

The intrinsic design space for the 24 mm GaN power device from 1.7-2.3 GHz for fundamental source ( $Z_{1S}$ ) and load ( $Z_{1L}$ ),

TABLE II  
INPUT NONLINEARITY PARAMETERS FOR THE REALIZED IN-PACKAGE SOURCE SECOND HARMONIC TERMINATIONS OF GAN 24 MM DEVICE

Frequency (MHz)	$\gamma$	$\phi_2$ (Degree)
1700	0.2	194
1800	0.18	187
1900	0.14	185
2000	0.1	189
2100	0	-
2200	0.15	300
2300	0.57	265

3.4-4.6 GHz for second harmonic source ( $Z_{2S}$ ) and load ( $Z_{2L}$ ), and 5.1-6.9 GHz for the third harmonic load ( $Z_{3L}$ ) is shown in Fig. 12(a) and 12(b). The design space is implemented by in-package harmonic terminations. It can be inferred that the second harmonic load impedance is reactive near short while the third harmonic load is near open confirming continuous class-F PA design space. For source, the input harmonics are terminated to be in a region where  $\gamma$  and  $\phi_2$  are favorable to

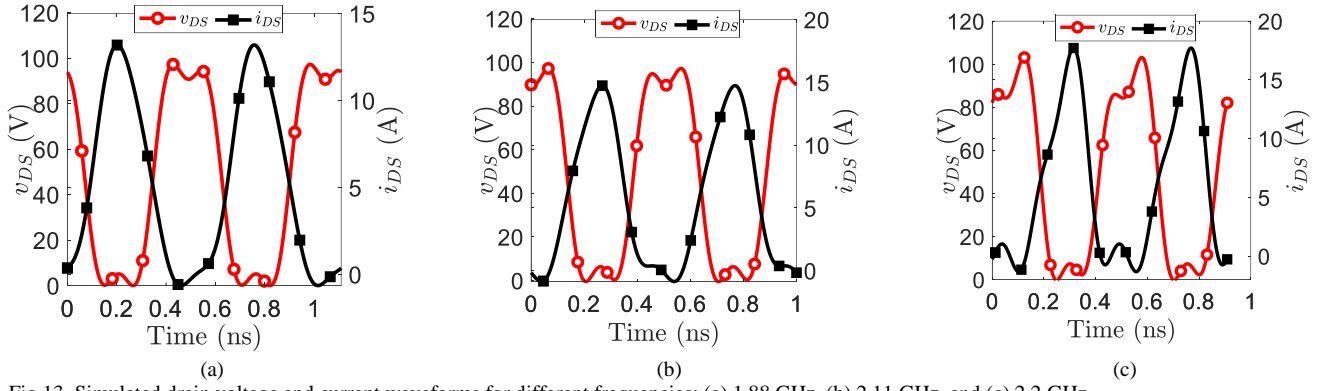


Fig.13. Simulated drain voltage and current waveforms for different frequencies: (a) 1.88 GHz, (b) 2.11 GHz, and (c) 2.2 GHz.

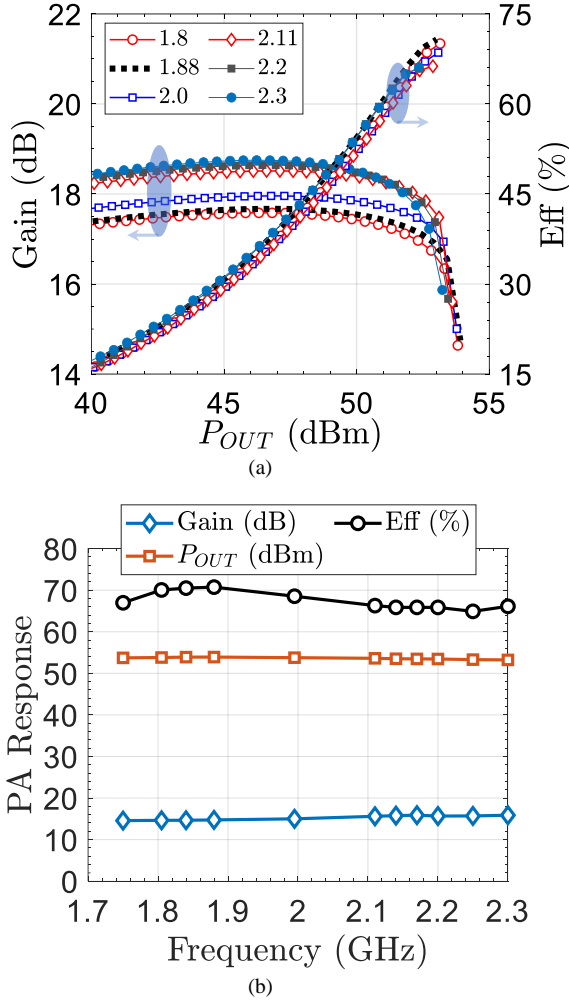


Fig. 14. (a) Power sweep at different frequencies, and (b) gain, efficiency and output power across 1.75-2.3 GHz.

shape input waveforms for optimum efficiency performance. The  $Z_{2S}$  terminations are designed around the region where efficiency deviation is minimum compared to the  $Z_{2S}$  short termination as can be inferred comparing Fig. 8(a-c) and Fig. 12(a). It is worth noting that the second harmonic source impedance is kept away of the efficiency minima at the input to achieve higher bandwidth. The input nonlinearity parameters ( $\gamma$  and  $\varphi_2$ ) are listed in Table II at different frequency points for the realized in-package  $Z_{2S}$  terminations. For CW measurement a high power load pull of this continuous class-F part was

TABLE III  
PERFORMANCE OF THE PROPOSED BROADBAND PA COMPARED TO THE PREVIOUS WORKS

Ref.	Year	Tech.	Freq. (GHz)	Pout (dBm)	Peak Eff. (%)
<b>This Work</b>	<b>2020</b>	<b>GaN</b>	<b>1.75-2.3</b>	<b>53.4-54</b>	<b>65-70.7</b>
[36]	2009	GaN	2.6	52.5	65.6
[37]	2017	GaN	1.7-2.7	52.7-54.3	55-65
[38]	2018	GaN	1.8-2.7	53.53.5	50-68
[39]	2016	GaN	1.55-1.6	54.7	55
[40]	2014	GaN	1.75-2.17	51	71-75
[41]	2014	GaN	2.14	54	70

performed and the corresponding output power and efficiencies are plotted in Fig. 12(c-e). With a 48 V drain and a -2.8 V gate supply voltage, the GaN 24 mm prematch part provides maximum output power (MXP) of 53.9 dBm (245 W) with  $Z_{L,MXP} = 4.9 - j12.2$  and maximum drain efficiency (MXE) of 70.7 % with  $Z_{L,MXE} = 8 - j10$  at 1.88 GHz as shown in Fig. 12(c). Likewise, at 2.11 GHz, MXP of 53.6 dBm at  $Z_{L,MXP} = 5.3 - j14$  and MXE of 66.3 % with  $Z_{L,MXE} = 6.9 - j11.2$  was measured as shown in Fig. 12(d). In addition, at 2.2 GHz, loading of  $Z_{L,MXP} = 5.4 - j14.8$  provides MXP of 53.4 dBm and  $Z_{L,MXE} = 6.3 - j10.8$  efficiency of 65.9 % as in Fig. 12(e). The intrinsic drain voltage and current waveforms for 1.88, 2.11 and 2.2 GHz are plotted for 24 mm GaN part in Fig. 13(a-c). The drain current waveform is half sinusoidal and a square voltage at 1.88 GHz confirms the class-F PA mode of operation. The peak voltage swing of 110 V ( $2.2 \times V_{DD}$ ) indicates continuous class-F mode voltage peaks to the right-hand side due to reactive second harmonic load termination as shown in Fig. 13(c).

The power sweep results at different frequency points in terms of drain efficiency (DE) for constant 3-dB gain compression level from 1.8 to 2.3 GHz (30% fractional bandwidth) are shown in Fig. 14(a). The frequency response of the 24 mm prematch device with 70.7% peak DE at 1.88 GHz, with a minimum efficiency of 65% from 1.75-2.3 GHz, maintaining an efficiency flatness of 6% across the band. The maximum output power at 3-dB gain compression is measured from 53.2-53.9 dBm. In addition, the large-signal gain at MXP with 3-dB compression varies from 14.5-15.9 dB across the band thereby providing a high gain flatness which is critical for high power cellular base station applications. The performance of the proposed input harmonic controlled broadband Class-F

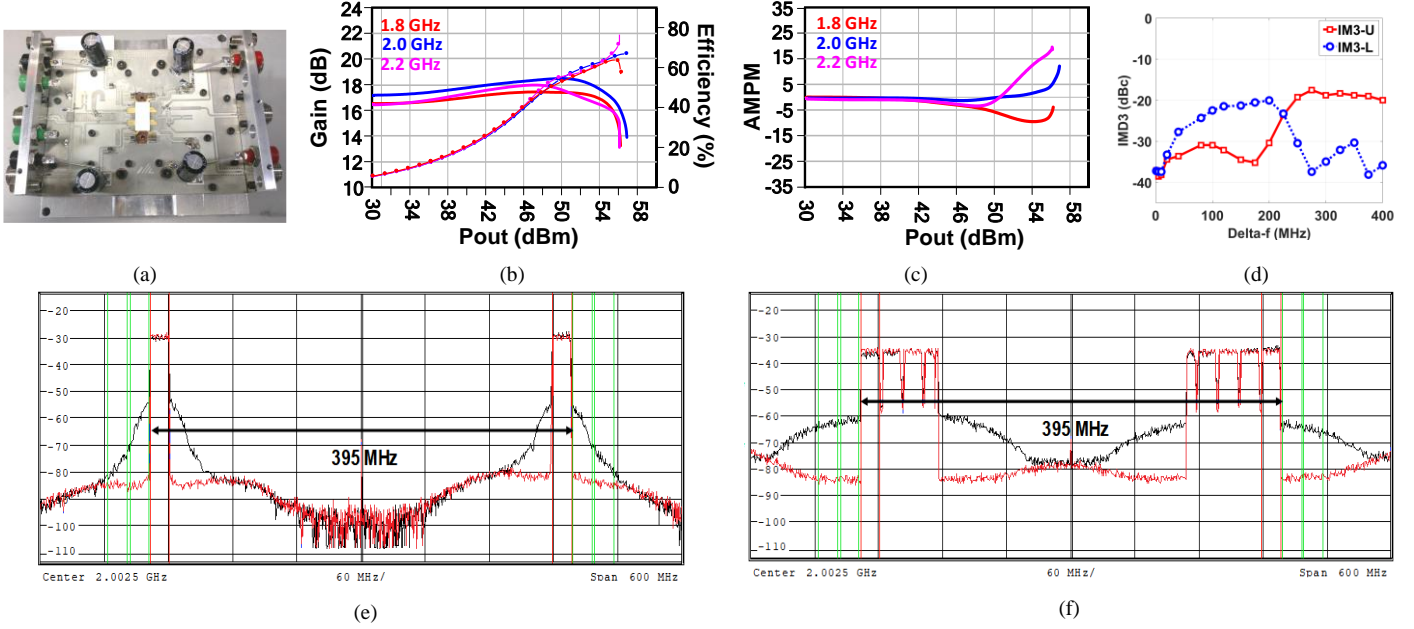


Fig 15. (a) Prototype of the symmetric doherty using GaN 24 mm prematch part, (b) gain and efficiency, (c) AMPM performance of the symmetric Doherty PA with output power, (d) IMD3 performance at constant 48 dBm output power, output spectrum with (red) and without (dark) digital predistortion for (c) LTE 2-carrier 20 MHz signal, and (d) LTE 10-carrier 20,10,5 MHz signal.

design is reported in Table III compared to the previous works [36]–[41]. It should be noted that the prematch device is implemented with in-package input-output harmonic terminations unlike previous works but provides comparable performance with excellent output power and gain flatness. This 24 mm GaN part is thereafter used in the design of a symmetric Doherty to demonstrate the modulated performance of the device.

### B. High Power Symmetric Doherty PA Design

To demonstrate wideband RF performance for modulated signal applications, a symmetric Doherty PA was designed and fabricated using the prematched part presented in Section IV. As such, the harmonic terminations are like what is shown in Fig. 12(a) and 12(b). The 50  $\Omega$  input-output printed circuit board (PCB) is realized using a low loss 20-mil Rogers substrate (RO4350) with a relative permittivity of 3.66. The dimensions of the Doherty circuit is approximately 10x6 cm<sup>2</sup>, as shown in Fig. 15(a). The gain, efficiency and AMPM response of the Doherty PA with output power are shown in Fig. 15(b) and 15(c). The Doherty PA is optimized for the best linearizable efficiency performance which is crucial in high power base-station applications. The symmetric Doherty with the pre-matched GaN part was tested using an LTE signal with the peak to average ratio (PAR) of 7.2 dB. The digital pre-distortion (DPD) was performed using wideband transceiver with 737.28 mega samples per second (MSPS) rate.

The symmetric Doherty PA was designed to realize desired wideband instantaneous bandwidth (IBW) of 395 MHz. A two-tone measurement was performed to capture the third order intermodulation distortion (IMD) for the Doherty PA at constant 48 dBm output power at different tone spacing as shown in Fig. 15(d). The PA demonstrates the lower IMD3 (IM3-L) and the upper IMD3 (IM3-U) well controlled lower than -17 dBc.

For a 2-carrier testing, 20 MHz LTE signal with instantaneous signal bandwidth (ISBW) varying between 200

TABLE IV  
DPD RESULTS WITH 2-CARRIER 20 MHz LTE SIGNAL

ISBW (MHz)	AE (%)	PB <sub>out</sub> (dBm)	ACPR-L (dBc)	ACPR-U (dBc)
200	45.2	47.5	-58	-57.1
250	44.3	47.3	-57	-56.4
300	45.8	47.6	-57.1	-56.7
365	46	47.5	-55	-54.1
395	44.3	47.3	-54.1	-52.3

ISBW: Instantaneous Signal Bandwidth, AE: Average Efficiency, PB<sub>out</sub>: output power at back-off, ACPR-L/R: Adjacent channel power ratio left/right.

and 395 MHz was used. Measured average efficiency, average output power, and corrected adjacent channel power ratio are reported in Table IV. The Doherty PA provides an average efficiency of 44.3–46% at 8 dB back-off with a corrected ACPR of -52 to -58 dBc. The average output power is higher than 47.3 dBm. The raw and corrected spectrum for the 2-carrier LTE test with 395 MHz ISBW is shown in Fig. 15(e). Furthermore, the DPD measurement was performed with a 10 carrier LTE signal consisting of 7x20 MHz carriers, 2x10 MHz carriers, and a single 5 MHz carrier and the achieved average efficiency is 46% at 48.8 dBm average output power with a corrected ACPR of -47 dBc as shown in Fig. 15(f).

### V. CONCLUSIONS

This work presents an in-depth analysis of a broadband class-F PA operation under the influence of input nonlinearity. The regions of second harmonic source terminations are identified that result in device conduction angle expansion or contraction. Thereafter, it has been investigated with new time-domain analyses that the continuity of a continuous class-F PA is in fact conditional to the input second harmonic terminations. As such, it is important to carefully consider the input second harmonic design space for the optimum broadband operation of a class-F PA. The analyses are validated with pulsed VLP measurements with a low power GaN device and

the optimum input second harmonic design space is identified. Further, a wideband high power GaN 24 mm part with in-package second harmonic source terminations is implemented as a proof of concept operating at 1.7-2.3 GHz. Finally, the GaN 24 mm part is used to build a symmetric Doherty PA with an IBW of 395 MHz providing average efficiency higher than 44% at 8 dB back-off.

## REFERENCES

- [1] A. Grebennikov and F. H. Raab, "History of Class-F and Inverse Class-F Techniques: Developments in High-Efficiency Power Amplification from the 1910s to the 1980s," *IEEE Microw. Mag.*, vol. 19, no. 7, pp. 99–115, Nov. 2018.
- [2] P. Colantonio, F. Giannini, and E. Limiti, *High Efficiency RF and Microwave Solid State Power Amplifiers*. John Wiley & Sons, 2009.
- [3] F. H. Raab, "Class-F power amplifiers with maximally flat waveforms," *IEEE Trans. Microw. Theory Tech.*, vol. 45, no. 11, pp. 2007–2012, Nov. 1997.
- [4] P. Colantonio, F. Giannini, G. Leuzzi, and E. Limiti, "Multiharmonic manipulation for highly efficient microwave power amplifiers," *Int. J. RF Microw. Comput.-Aided Eng.*, vol. 11, no. 6, pp. 366–384, Nov. 2001.
- [5] F. H. Raab, "Maximum efficiency and output of class-F power amplifiers," *IEEE Trans. Microw. Theory Tech.*, vol. 49, no. 6, pp. 1162–1166, Jun. 2001.
- [6] P. J. Tasker, "Practical waveform engineering," *IEEE Microw. Mag.*, vol. 10, no. 7, pp. 65–76, Dec. 2009.
- [7] J. H. Kim, G. D. Jo, J. H. Oh, Y. H. Kim, K. C. Lee, and J. H. Jung, "Modeling and Design Methodology of High-Efficiency Class-F and Class-F<sup>-1</sup> Power Amplifiers," *IEEE Trans. Microw. Theory Tech.*, vol. 59, no. 1, pp. 153–165, Jan. 2011.
- [8] J. Moon, S. Jee, J. Kim, J. Kim, and B. Kim, "Behaviors of Class-F and Class-F<sup>-1</sup> Amplifiers," *IEEE Trans. Microw. Theory Tech.*, vol. 60, no. 6, pp. 1937–1951, Jun. 2012.
- [9] T. Sharma *et al.*, "Simplified First-Pass Design of High-Efficiency Class-F<sup>-1</sup> Power Amplifiers Based on Second-Harmonic Minima," *IEEE Trans. Microw. Theory Tech.*, pp. 1–15, 2019.
- [10] T. Sharma *et al.*, "Novel High Efficiency Power Amplifier Mode Using Open Circuit Harmonic Loading," in *2019 IEEE MTT-S International Microwave Symposium (IMS)*, 2019, pp. 79–82.
- [11] P. Colantonio, F. Giannini, G. Leuzzi, and E. Limiti, "Theoretical facet and experimental results of harmonic tuned PAs," *Int. J. RF Microw. Comput.-Aided Eng.*, vol. 13, no. 6, pp. 459–472, Oct. 2003.
- [12] S. C. Cripps, P. J. Tasker, A. L. Clarke, J. Lees, and J. Benedikt, "On the Continuity of High Efficiency Modes in Linear RF Power Amplifiers," *IEEE Microw. Wirel. Compon. Lett.*, vol. 19, no. 10, pp. 665–667, Oct. 2009.
- [13] P. Wright, J. Lees, J. Benedikt, P. J. Tasker, and S. C. Cripps, "A Methodology for Realizing High Efficiency Class-J in a Linear and Broadband PA," *IEEE Trans. Microw. Theory Tech.*, vol. 57, no. 12, pp. 3196–3204, Dec. 2009.
- [14] V. Carrubba *et al.*, "On the Extension of the Continuous Class-F Mode Power Amplifier," *IEEE Trans. Microw. Theory Tech.*, vol. 59, no. 5, pp. 1294–1303, May 2011.
- [15] V. Carrubba *et al.*, "The Continuous Inverse Class-F Mode With Resistive Second-Harmonic Impedance," *IEEE Trans. Microw. Theory Tech.*, vol. 60, no. 6, pp. 1928–1936, Jun. 2012.
- [16] N. Tuffy, L. Guan, A. Zhu, and T. J. Brazil, "A Simplified Broadband Design Methodology for Linearized High-Efficiency Continuous Class-F Power Amplifiers," *IEEE Trans. Microw. Theory Tech.*, vol. 60, no. 6, pp. 1952–1963, Jun. 2012.
- [17] S. Rezaei, L. Belostotski, F. M. Ghannouchi, and P. Aflaki, "Integrated Design of a Class-J Power Amplifier," *IEEE Trans. Microw. Theory Tech.*, vol. 61, no. 4, pp. 1639–1648, Apr. 2013.
- [18] S. Rezaei, L. Belostotski, M. Helaoui, and F. M. Ghannouchi, "Harmonically Tuned Continuous Class-C Operation Mode for Power Amplifier Applications," *IEEE Trans. Microw. Theory Tech.*, vol. 62, no. 12, pp. 3017–3027, Dec. 2014.
- [19] T. Sharma, R. Darraji, and F. Ghannouchi, "A Methodology for Implementation of High-Efficiency Broadband Power Amplifiers With Second-Harmonic Manipulation," *IEEE Trans. Circuits Syst. II Express Briefs*, vol. 63, no. 1, pp. 54–58, Jan. 2016.
- [20] T. Sharma, R. Darraji, F. Ghannouchi, and N. Dawar, "Generalized Continuous Class-F Harmonic Tuned Power Amplifiers," *IEEE Microw. Wirel. Compon. Lett.*, vol. 26, no. 3, pp. 213–215, Mar. 2016.
- [21] Z. Lu and W. Chen, "Resistive Second-Harmonic Impedance Continuous Class-F Power Amplifier With Over One Octave Bandwidth for Cognitive Radios," *IEEE J. Emerg. Sel. Top. Circuits Syst.*, vol. 3, no. 4, pp. 489–497, Dec. 2013.
- [22] M. Yang, J. Xia, Y. Guo, and A. Zhu, "Highly Efficient Broadband Continuous Inverse Class-F Power Amplifier Design Using Modified Elliptic Low-Pass Filtering Matching Network," *IEEE Trans. Microw. Theory Tech.*, vol. 64, no. 5, pp. 1515–1525, May 2016.
- [23] S. Y. Zheng, Z. W. Liu, X. Y. Zhang, X. Y. Zhou, and W. S. Chan, "Design of Ultrawideband High-Efficiency Extended Continuous Class-F Power Amplifier," *IEEE Trans. Ind. Electron.*, vol. 65, no. 6, pp. 4661–4669, Jun. 2018.
- [24] X. Li, M. Helaoui, and X. Du, "Class-X–Harmonically Tuned Power Amplifiers With Maximally Flat Waveforms Suitable for Over One-Octave Bandwidth Designs," *IEEE Trans. Microw. Theory Tech.*, vol. PP, no. 99, pp. 1–12, 2018.
- [25] P. Colantonio, F. Giannini, G. Leuzzi, and E. Limiti, "High efficiency low-voltage power amplifier design by second-harmonic manipulation," *Int. J. RF Microw. Comput.-Aided Eng.*, vol. 10, no. 1, pp. 19–32, Dec. 1999.
- [26] T. Sharma *et al.*, "High-Efficiency Input and Output Harmonically Engineered Power Amplifiers," *IEEE Trans. Microw. Theory Tech.*, vol. PP, no. 99, pp. 1–13, 2017.
- [27] P. M. White, "Effect of input harmonic terminations on high efficiency class-B and class-F operation of PHEMT devices," in *1998 IEEE MTT-S International Microwave Symposium Digest (Cat. No.98CH36192)*, 1998, vol. 3, pp. 1611–1614 vol.3.
- [28] T. Canning, P. Tasker, and S. Cripps, "Waveform Evidence of Gate Harmonic Short Circuit Benefits for High Efficiency X-Band Power Amplifiers," *IEEE Microw. Wirel. Compon. Lett.*, vol. 23, no. 8, pp. 439–441, Aug. 2013.
- [29] S. K. Dhar, T. Sharma, N. Zhu, D. Holmes, R. Darraji, and F. M. Ghannouchi, "Comprehensive Analysis of Input Waveform Shaping for Efficiency Enhancement in Class B Power Amplifiers," in *2019 IEEE MTT-S International Microwave Symposium (IMS)*, 2019, pp. 1164–1167.
- [30] A. Alizadeh and A. Medi, "Investigation of a Class-J Mode Power Amplifier in Presence of a Second-Harmonic Voltage at the Gate Node of the Transistor," *IEEE Trans. Microw. Theory Tech.*, vol. 65, no. 8, pp. 3024–3033, Aug. 2017.
- [31] M. Haynes, S. C. Cripps, J. Benedikt, and P. J. Tasker, "PAE improvement using 2nd harmonic source injection at x-band," in *2012 Workshop on Integrated Nonlinear Microwave and Millimetre-wave Circuits*, 2012, pp. 1–3.
- [32] G. Bosi, A. Raffo, G. Vannini, E. Cipriani, P. Colantonio, and F. Giannini, "Gate waveform effects on high-efficiency PA design: An experimental validation," in *2014 9th European Microwave Integrated Circuit Conference*, 2014, pp. 329–332.
- [33] S. K. Dhar *et al.*, "Investigation of Input–Output Waveform Engineered Continuous Inverse Class F Power Amplifiers," *IEEE Trans. Microw. Theory Tech.*, vol. 67, no. 9, pp. 3547–3561, Sep. 2019.
- [34] "Focus Device Characterization Suite (FDCS)." [Online]. Available: <https://focus-microwaves.com/fdcs/>.
- [35] N. Zhu, R. McLaren, J. S. Roberts, D. G. Holmes, M. Masood, and J. K. Jones, "Compact High-Efficiency High-Power Wideband GaN Amplifier Supporting 395 MHz Instantaneous Bandwidth," in *2019 IEEE MTT-S International Microwave Symposium (IMS)*, 2019, pp. 1175–1178.
- [36] H. Deguchi, N. Ui, K. Ebihara, K. Inoue, N. Yoshimura, and H. Takahashi, "A 33W GaN HEMT Doherty amplifier with 55% drain efficiency for 2.6GHz base stations," in *2009 IEEE MTT-S International Microwave Symposium Digest*, 2009, pp. 1273–1276.
- [37] X. Chen, W. Chen, Q. Zhang, F. M. Ghannouchi, and Z. Feng, "A 200 watt broadband continuous-mode doherty power amplifier for base-station applications," in *2017 IEEE MTT-S International Microwave Symposium (IMS)*, 2017, pp. 1110–1113.
- [38] H. Jang and R. Wilson, "A 225 Watt, 1.8-2.7 GHz Broadband Doherty Power Amplifier with Zero-Phase Shift Peaking Amplifier," in *2018 IEEE/MTT-S International Microwave Symposium - IMS*, 2018, pp. 797–800.
- [39] R. Giorfrè, P. Colantonio, L. Gonzalez, L. Cabria, and F. De Arriba, "A 300W complete GaN solid state power amplifier for positioning system



satellite payloads,” in *2016 IEEE MTT-S International Microwave Symposium (IMS)*, 2016, pp. 1–3.

- [40] J. Son, Y. Park, I. Kim, J. Moon, and B. Kim, “Broadband Saturated Power Amplifier With Harmonic Control Circuits,” *IEEE Microw. Wirel. Compon. Lett.*, vol. 24, no. 3, pp. 185–187, Mar. 2014.
- [41] I. Takenaka *et al.*, “High-Efficiency and High-Power Microwave Amplifier Using GaN-on-Si FET With Improved High-Temperature Operation Characteristics,” *IEEE Trans. Microw. Theory Tech.*, vol. 62, no. 3, pp. 502–512, Mar. 2014.



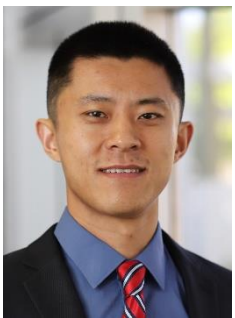
**Sagar K. Dhar** (S'11) is currently pursuing his Ph.D. degree at the iRadio Lab, University of Calgary, Calgary, AB, Canada. His current research interests include high-efficiency RF power amplifiers, RF Front-Ends, MMIC, Active and Passive RF circuits and systems, and load-pull techniques. He has authored or co-authored over 20 refereed publications and holds 3 US patents.

Mr. Dhar was a recipient of the Izaak Walton Killam Pre-Doctoral Scholarship, the AITF Doctoral Scholarship, the Open Doctoral Scholarship, the Transformative Talent Internship Award, the Academic Excellence Award, and the Research Productivity Award.



**Tushar Sharma** (S'10) is a postdoctoral research associate at Princeton University, NJ, USA. He received his Ph.D. degree from the University of Calgary, Alberta in 2018 in the area of high-efficiency power amplifier design. In 2016–2018, he joined NXP Semiconductors, USA as a research and development RF engineer to work in the field of gallium nitride technology characterization and RF power amplifier design for 5G base station application. His research areas include mm-wave (30–100 GHz) advanced transmitter architectures in CMOS, GaN, InP,

high power (50–300 W) broadband amplifiers for cellular infrastructure, device characterization, waveform engineering-based harmonic tuned PAs etc. Dr. Sharma is a recipient of the Izaak Walton Killam Pre-Doctoral Scholarship, Alberta Science and Innovation under 30 Future leader award, the AITF Doctoral Scholarship, the Alberta Transformative Talent scholarship, the Academic Excellence Award, and the Research Productivity Award. He has authored and coauthored over 25 refereed publications and 2 pending US patents.



**Ning Zhu** (S'10, M'13) received the B.Sc. and M.Sc. degrees from the University of Electronic Science Technology of China, Chengdu, Sichuan, China, in 2006 and 2009, respectively, and the Ph.D. degree from the University of Arizona, Tucson, AZ, in 2013. Since then, he has been with Radio Power Solutions, NXP Semiconductors, Chandler, AZ, USA. He has authored and co-authored over 30 technical publications and 18 U.S. patents, awarded and pending. His research interests include high-efficiency power amplifiers, RF/mmW antennas, power harvesting, and frequency synthesis.



**Ramzi Darraji** (S'10, M'13) received the M.Sc. degree in communications engineering from the École Supérieure des Communications de Tunis, Ariana, Tunisia, in 2008 and the Ph.D. degree in electrical engineering from the University of Calgary, Calgary, AB, Canada, in 2013.

He is currently with Ericsson Canada Inc., Ottawa, ON, Canada. He has authored and co-authored over 50 refereed publications and holds 4 patents. His current research interests include advanced power amplifier design and wireless RF front-end systems for cellular base

transceiver stations.



**Roy McLaren** (M' 20) received the M.Eng. degree from Heriot-Watt University, Edinburgh, UK, in 1990. He has over 25 years industrial experience, and from 1995–2012 worked with Ericsson Radio Systems, Nokia and ZTE Corporation as an RF specialist with focus on high-power macro-cell power amplifier product development and R&D for cellular communications. Since 2012 he has worked with Freescale and NXP Semiconductors, Chandler AZ, USA, where he is currently the technical lead for power amplifier architectures and hardware within NXP's Technology and Innovations business line. His primary focus areas include new and emerging power amplifier architectures and broadband multi-band Doherty PA's for mid-power massive-MIMO and high-power cellular applications. He holds 15 patents, awarded and pending.



**Damon G. Holmes** (M' 13) received the B.Sc. and M.Sc. degrees from the University of Calgary, Calgary, AB, Canada, in 2002 and 2005, respectively. He has gained over 15 years of industrial experience with Nortel Networks Wireless Infrastructure Group, Freescale and NXP Semiconductors, Chandler, AZ, USA, pursuing product development for transmitter architectures, advanced power amplifier design including Doherty, waveform shaping and large signal device modeling in support of cellular and wireless communication technology. He

currently manages the New Technology Integration RF design efforts for cellular applications at NXP Semiconductors' Radio Power Solutions business unit. He has authored or co-authored over 20 refereed publications and has over 30 patents, awarded or pending.



**Vince Mallette** is currently the Director of sales and business development at Focus Microwaves, Montreal, Canada. He has over 12 years of experience in international sales, marketing and strategic business development in Test and Measurement. His current interests include global strategic sales and marketing initiatives and expansion in new markets as well as continued expansion among existing clients.



**Fadhel M. Ghannouchi** (S'84–M'88–SM'93–F'07) is currently a professor, Alberta Innovates/Canada Research Chair and Director of the iRadio Laboratory in the Department of Electrical and Computer Engineering at the University of Calgary, Alberta, Canada and a part-time Thousand Talent Professor at Department of Electronics Engineering, Tsinghua University, Beijing China. His research interests are in the areas of RF and wireless communications, nonlinear modeling of microwave devices and communications

systems, design of power- and spectrum-efficient microwave amplification systems and design of SDR systems for wireless, optical and satellite communications applications. He is Fellow of the Academy of Science of the Royal Society of Canada, Fellow of the Canadian Academy of Engineering, Fellow of the Engineering Institute of Canada, Fellow of the Institution of Engineering and Technology (IET) and Fellow of the Institute of Electrical and Electronic Engineering (IEEE). He published more than 800 referred papers, 6 books and hold 25 patents (3 pending). Prof. Ghannouchi is the co-founder of three university spun-off companies.